Control of Corrosion Resistance and Osteoclastic Resorbability of Bioresorbable Carbonate Apatite Coating for Biodegradable Mg Alloys through Carbonate Content

Sachiko Hiromoto [a,b,*], *Kazuma Midorikawa* [a,b,†], *Tomohiko Yamazaki* [c] *and Tomoyuki Yamamoto* [b,d]

a Research Center for Structural Materials, National Institute for Materials Science, Tsukuba 305-0047, Japan

b Faculty of Science and Engineering, Waseda University, Tokyo, 169-8555, Japan

c Research Center for Macromolecules and Biomaterials, National Institute for Materials Science, Tsukuba, 305-0047, Japan

d Kagami Memorial Research Institute for Materials Science and Technology, Tokyo 169-0051, Japan

† Present Affiliation: Nippon Steel Corporation

ABSTRACT

To investigate the effect of carbonate content on the corrosion resistance and osteoclastic resorbability of carbonate apatite (CAp) coatings for biodegradable Mg alloys, polarization, electrochemical impedance (EI), and osteoclast precursor cell culture tests were conducted for CAp-coated pure Mg (Mg) and Mg-4Y-3RE (WE43) containing approximately 11, 17, and 18 wt% carbonate. In Hanks' solution, the polarization resistance (R_p) was higher than in 0.9% NaCl solution, and the CAp coatings improved the R_p of Mg by 7 to 15 times. The R_p of CAp-coated Mg increased by approximately 1.5 times in 0.9% NaCl solution and 2 times in Hanks' solution with increasing carbonate content, indicating a reduction in coating defects. For CAp-coated Mg, osteoclasts only survived on higher carbonate content coating. For WE43, the coating with higher carbonate content exhibited a higher number of mature osteoclasts and approximately a 1.5-fold increase in the resorbed area by osteoclasts. These findings demonstrate that the carbonate content in the CAp coating allows for the adjustment of the corrosion rate of biodegradable Mg alloys to suit the affected part of the body. It was also found that once osteoclasts are induced, the CAp coating with higher carbonate content is resorbed more quickly by the osteoclasts.

KEYWORDS: carbonate apatite coating, carbonate content, corrosion, bioabsorption, biomedical magnesium alloys, calcium phosphate

1. Introduction

Magnesium (Mg) and Mg alloys are a highly potential biodegradable metallic material as well as Zn and Fe alloys for orthopedic, dental, and circulatory devices, such as bone fixation screws and plates, pins, staples, mesh plates, stents and so on, due to their good biocompatibility and mechanical compatibility [1-9]. However, Mg/Mg alloys sometimes show too rapid corrosion in the early stages of implantation, leading to early degradation of mechanical integrity, gas cavity formation due to hydrogen (H_2) gas, and pH increase caused by OH^- ions [10-17]. Gas cavities may interfere with tissue generation although the cavities eventually disappear as they are filled with the surrounding tissues [18]. The healing time of an affected body part depends on its location, as well as on the patient's health condition and age, since bone healing can be delayed by factors such as aging, a smoking history, and underlying conditions such as diabetes [19, 20]. Mg alloy devices are expected to be used in various anatomical sites, including around bone, inside blood vessels, and in intestines, each of which presents a distinct corrosion environment. The required periods for medical devices to provide load-bearing or suture retention depend on factors such as the anatomical site, patient condition, and the local corrosion environment. Therefore, the corrosion rate of the Mg alloy devices should be adjusted accordingly.

To suppress the corrosion of Mg/Mg alloys, various types of coatings, such as calcium phosphate, other phosphate compounds, MgF_2, bio-glasses, TiO_2 and composite coatings have been developed. These coatings are typically fabricated using methods such as chemical conversion, micro-arc oxidation (MAO), sol-gel processing, and ion implantation [3, 6, 8, 21-29]. In particular, calcium phosphate coatings, such as hydroxyapatite (HAp), β-tricalcium phosphate (β-TCP), calcium phosphate dihydrate (DCPD), and amorphous calcium phosphate coatings, have received significant attention owing to their excellent biocompatibility. Among calcium

phosphates, HAp and carbonate apatite (CAp) have drawn special interest for the following reasons. HAp is used as an artificial bone substitute and as a bone conductive coating for artificial joints and dental implants [30-32]. Additionally, CAp was recently approved as a bioabsorbable artificial bone substitute as Cytrans Granules® (GC Corporation, Tokyo, Japan) [33], and a Ca-deficient CAp coating is used for Ti alloy devices [34, 35]. Furthermore, CAp can be absorbed by osteoclasts in hard tissue and replaced with bone [33], and can also be resorbed by osteoclast-like cells in soft tissue [36]. Therefore, the CAp coating is expected to function as a bioabsorbable coating which provides effective corrosion protection for substrate Mg alloys until osteoclasts or osteoclast-like cells are induced and secrete acids to resorb CAp.

We have developed HAp and CAp coatings whose crystallinity, thickness and carbonate content can be varied by coating conditions such as pH, temperature and carbonate salt concentration of the coating solution and coating time [37-39], and revelaed that the corrosion resistance of the HAp-coated Mg alloys varied with the coating conditions [40-42]. In a rabbit femoral implantation study for CAp-coated Mg-Ca alloy plates and screws, we found that dissolution of the CAp coating occurred at the surfaces where new bone had formed [43].

In the CAp coatings, the thickness of the CAp layer decreases with increasing its carbonate content [38, 39], and it has been reported that the solubility of CAp increases as the carbonate content rises [44, 45]. Therefore, adjusting the carbonate content is expected to offer a means of controlling the corrosion of CAp-coated Mg alloys. To achieve effective regulation via carbonate content, it is crucial to understand the effect of the carbonate content on the corrosion resistance and the osteoclastic resorption behavior of the CAp coating on the surfaces of Mg and its alloys. The resorption behavior of the CAp coating may be influenced by the corrosion of the underlying Mg substrate through an increase in pH, since Mg corrosion raises the surface pH, while osteoclastic

resorption of CAp is facilitated by the acid produced by osteoclasts. Previously, we reported that the CAp coating with the higher carbonate contents can possibly show higher corrosion resistance for Mg-4Y-3RE (WE43) in medium [46], while the effect of the carbonate content on the osteoclastic resorption behavior was not clarified. It was found that, with carbonate ion source concentrations of 0.4, 1.1, and 1.9 mol/L in this previous study [46], the carbonate content of the CAp coating was saturated at 20–25 wt% at concentrations above 1.0 mol/L [39]. Moreover, this carbonate content range is higher than the 10 to 20 wt% found in bone apatite [47]. Therefore, it should be said that the previous concentrations were not necessarily suitable for investigating the influence of carbonate content.

In this study, the effect of the carbonate content in the CAp coating on the corrosion behavior and osteoclastic resorption ability was investigated using CAp-coated pure Mg samples with approximately 11, 17, and 18 wt% carbonate contents. Polarization, electrochemical impedance (EI), and osteoclast cell culture tests were performed. An HAp coating was used as a comparison in the electrochemical corrosion tests. In osteoclast cell culture tests, CAp-coated WE43 samples were additionally used because the corrosion rate of the CAp-coated pure Mg was sometimes too high to allow cell evaluation. The composition and structure of the CAp coatings used in this study have already been investigated in detail in our previous publication [39], and thus are not repeated here.

2. Materials and methods

2.1. CAp and HAp coating of pure Mg and WE43

Pure Mg (99.95%, Osaka Fuji Corp.) and Mg-4Y-3RE (WE43) (Magnesium Electron) disks with a diameter of 15 mm or 16 mm and a thickness of 2 mm were prepared from extruded rods. The surface of disks was ground with SiC papers (PSI, USA) up to #1200 and rinsed ultrasonically in 2-propanol. The compositions of pure Mg and WE43 are shown in Table 1.

The CAp coatings were prepared according to the procedure described in our previous study [39]. A solution containing 0.2 mol/L ethylenediaminetetraacetic acid calcium disodium salt hydrate ($C_{10}H_{12}CaN_2Na_2O_8 \cdot xH_2O$) solution, 0.2 mol/L potassium dihydrogen phosphate (KH_2PO_4), and 0.2 mol/L NaOH was prepared and the pH was checked to be between 8 and 9. Then, sodium hydrogen carbonate ($NaHCO_3$) was added to this solution to obtain final concentrations of 0, 0.25, 0.5, and 1.0 mol/L. Pure Mg and WE43 disks were immersed in the coating solutions at 363 K for 3.6 ks. The coated samples were generally named according to the $NaHCO_3$ concentrations and the substrate alloy as HAp-Mg, CAp0.25-Mg, CAp0.5-Mg, and CAp1.0-Mg and CAp0.25-WE43, CAp0.5-WE43, and CAp1.0-WE43. The carbonate content of CAp0.25, CAp0.5, and CAp1.0 coatings was approximately 11, 17, and 18 wt%, respectively for pure Mg and WE43, according to the previous study, since it was found that the carbonate content is independent of the substrate type [39].

Surface and cross section of the coated samples were observed using scanning electron microscope (SEM) (JSM6500F, JEOL). The crystal structure of the coatings was identified with X-ray diffraction (XRD) (Smart-Lab, RIGAKU) using Cu Kα radiation (λ=0.15406 nm).

2.2. Potentiodynamic polarization and EI tests of HAp- and CAp-Mg

Potentiodynamic polarization and EI tests were carried out for HAp- and CAp-Mg in 0.9% NaCl and Hanks' solutions at 310 K. Each specimen disk was mounted on a specimen holder, exposing 1 cm^2 to the electrolyte. Ag/AgCl (3M KCl) and Pt electrodes were used as the reference and counter electrodes, respectively. In the anodic and cathodic polarization tests, open circuit potential (OCP) of the specimen was measured for 1.8 ks until the potential became nearly constant, then the potential was swept from 50 mV more negative or more positive than the OCP in the anodic or cathodic direction, respectively, at a potential sweep rate of 1 mV s^{-1}. In the EI tests, after the 1.8 ks-OCP measurement, the potential perturbation was applied with an amplitude of 5 mV at frequencies from 10 MHz to 10 mHz and with points per decade of 5. An equivalent electric circuit was assumed and curve-fitting for the measured EI spectra was performed to obtain the values of parameters in the circuit using Zview® (Scriber). Then, the polarization resistance (R_p) was calculated from the parameters in the circuit.

2.3. Osteoclast cell culture on CAp-Mg and WE43

Rat osteoclast precursors (OSC11, Cosmo Bio, Tokyo, Japan) were cultured on the CAp-Mg and WE43 with different carbonate contents. Glass disks with a diameter of 13 mm (Matsunami glass, Osaka, Japan) were used as the reference sample. The specimens were dipped in acetone for 10 s for sterilization and dried in air. On Day 0, before seeding cells, each specimen was placed in a well of a12-well plate and immersed in 2 mL of α-minimum essential medium (α-MEM; Thermo Fisher Scientific, Waltham, Massachusetts, USA) supplemented with 10% fetal bovine serum (FBS; Sigma-Aldrich, St Louis, Missouri, USA) at 310 K for 24 h in a 5% CO_2 incubator. On Day 1, the used medium was collected from each well, and osteoclast precursor cells were seeded at

4×10^4 cells/well with 4 mL of osteoclast culture medium (OSCMR, Cosmo Bio) containing 50 ng/mL macrophage colony stimulating factor (M-CSF) and 15 ng/mL receptor activator of NF-κB ligand (RANKL). RANKL induces the differentiation of osteoclast precursor cells to mature osteoclast cells. As osteoclast precursors differentiate and mature into osteoclasts, they become multinucleated and increase in size. Once matured, osteoclasts form an actin ring on the bone surface to which they adhered, producing acids within the ring to dissolve the bone. The cells were cultured for 3, 7, and 14 days (up to Days 4, 8, and 15) with a refreshment of osteoclast culture medium on Day 8.

On Days 4, 8, and 15, the cells were dehydrated and fixed to the specimen surface with methanol and then the cell bodies were stained with Giemsa (Muto Pure Chemicals, Japan) to observe the cell proliferation on the entire surface of the specimen disks. Concurrently, tartrate-resistant acid phosphate (TRAP) in differentiated osteoclast cells was stained using TRAP staining kit (AK04F, Cosmo Bio) to confirm the differentiation of precursors to osteoclasts. The Giemsa-stained and TRAP-stained specimens were observed using optical microscope (VHX-5000, Keyence, Japan). The surface morphology of the TRAP-stained specimens was analysed using a one-shot 3D profilometer (KEYENCE VR-3100). On Day 15, the cytoplasm of living cells and the nuclei of dead cells were stained with calcein in green and propidium iodide (PI) in red, respectively. The calcein-PI-stained cells were observed using a fluorescence microscope (DMIL-TR/EC3, Leica). Magnesium ions in the used medium collected on Days 1, 4, 8, and 15 were quantified by a colorimetric method using Magnesium B-test Wako (Wako Pure Chemical, Osaka, Japan). Three specimens from each sample were used for each cell culture period, and one specimen from each sample was used for Giemsa and TRAP staining, respectively. More than three specimens from each condition were used for quantification of Mg^{2+} ions.

The number of TRAP-positive cells and the mean cell size were obtained from optical images as follows. The optical images of 1.81 mm × 1.31 mm (2.46 mm^2) were taken at five fields of view at a magnification sufficient to distinguish cells from corrosion products. Then, the total number of TRAP-positive cells and the total area occupied by the cells in each field of view were determined using ImageJ (NIH). Subsequently, the values for each of the five fields of view were summed. The area occupied by cells was then divided by the number of cells to obtain the mean cell area. In addition, the area of the CAp coating resorbed by osteoclasts was measured using 3D images of the TRAP-stained specimens and further analyzed using low-magnification 3D images of the Giemsa-stained specimens. The measurement procedure is described later.

3. Results and Discussion

3.1. CAp coating of Mg and WE43

Figure 1(a)-(g) shows the surface and cross-sectional SEM images of HAp- and CAp-Mg, and the surface SEM images of CAp-WE43. Figure 1(h) shows the thickness of the HAp and CAp coatings obtained from the cross-sectional SEM images as a function of the carbonate content. Both on Mg and WE43, the CAp coating was composed of one layer of densely agglomerated dome-shaped particles consisting of sub-micrometer-sized particles. The thickness of the CAp coating decreased from approximately 1.8 to 1.1 μm with an increase in the carbonate content. The HAp coating composed of two layers of dense inner layer and porous outer layer with rod-shape particles and the thickness was about 2.2 μm. These results are consistent with the previous work [38, 39].

Figure 2(a-1) and (b-1) shows the wide range XRD patterns and Fig. 2(a-2) and (b-2) shows the magnified apatite 002 plane peak. For all the samples, diffraction peaks from apatite structure were observed at around 26, 28, 29, 33, 49, 51.5 and 53 degrees. CAp-Mg exhibited a shift in apatite 002 plane peak position at each $NaHCO_3$ concentration similar to that observed for CAp-WE43. This result indicates that the CAp coating on Mg had the same carbonate content as that on WE43. The presence of carbonate groups within the apatite structure was previously confirmed by Fourier transform infrared absorption measurements [39], as shown in Fig. S1.

3.2. Polarization behavior of HAp- and CAp-Mg

Figure 3(a)-(d) shows the anodic and cathodic polarization curves of HAp- and CAp-Mg in 0.9% NaCl and Hanks' solutions. Corrosion current density (I_{corr}) obtained from the polarization curves is shown in Fig. 3(e). In 0.9% NaCl solution, the cathodic current density of CAp-Mg was higher than that of HAp-Mg, and it increased with an increase in the carbonate content (Fig. 3(a)). The anodic current density near corrosion potential (E_{corr}) of CAp-Mg was apparently higher than that of HAp-Mg. Only CAp0.25-Mg exhibited a constant current region followed by a rapid current increase due to the breakdown of the CAp coating, whereas the other samples showed a gradual current increase from the E_{corr} up to the breakdown potential.

In Hanks' solution, the cathodic current density near the E_{corr} decreased in comparison to that in 0.9% NaCl solution for CAp-Mg. The anodic polarization curves in Hanks' solution showed a clear constant current region with a lower current density value than in 0.9% NaCl solution, leading to the lower I_{corr} values in Hanks' solution than those in 0.9% NaCl solution (Fig. 3(e)). After anodic polarization, several large corrosion pits were formed on the specimen surface in both

solutions. The SEM observation and energy dispersive X-ray spectroscopy (EDS) analysis revealed that in 0.9% NaCl solution, cracks and delamination of the HAp and CAp coatings were observed over almost the entire surface, and the surface was covered with $Mg(OH)_2$ corrosion products (Fig. S2(a, c) and Table S1). In contrast, in Hanks' solution, cracks and delamination of the coatings were not observed outside the corrosion pits, and corrosion products containing calcium phosphate were formed in the corrosion pits (Fig. S2(b, d) and Table S1). It was reported that calcium phosphates can readily precipitate as Mg corrodes in Hanks' solution [8, 48]. These facts indicate that calcium phosphate deposited to fill the defects in the HAp and CAp coatings in Hanks' solution, leading to the clear constant current region (Fig. 3(d)).

With an increase in the carbonate content, the I_{corr} in 0.9% NaCl increased, whereas that in Hanks' solution slightly decreased (Fig. 3(e)). The higher corrosion protectiveness associated with the higher carbonate content in the CAp coating was also suggested for WE43 in medium [46]. Considering that the CAp coating with the higher carbonate content was thinner (Fig. 1) and showed the higher I_{corr} in 0.9% NaCl solution (Fig. 3(e)), CAp-Mg with the higher carbonate content presumably exhibited a higher corrosion rate immediately after immersion in Hanks' solution, promoting the precipitation of calcium phosphates that could repair defects in the thin coating, ultimately enhancing the protective nature.

3.3. EI behavior of HAp- and CAp-Mg

Figure 4(a) and (b) shows the Nyquist plots of EI spectra of HAp- and CAp-Mg in 0.9% NaCl and Hanks' solutions. In both solutions, HAp- and CAp-Mg showed two flattened semicircles at medium and low frequencies, while the uncoated Mg showed one semicircle. Then, the R_p of the

uncoated Mg in 0.9% NaCl and Hanks' solutions was determined from the diameter of the semicircle as approximately 25 Ω· cm^2 and 15 kΩ· cm^2, respectively.

An equivalent electric circuit shown in Fig. 4(c) was then assumed for HAp- and CAp-Mg. Constant phase element (*CPE*) was used because of the flattened semicircles on the Nyquist plots and the microscopically rough surface of the apatite coatings (Fig. 1). R_s represents the solution resistance. R_{coat} corresponds to the resistance of the apatite coatings (solution resistance inside the apatite coatings), and CPE_{coat} represents the *CPE* of the apatite coatings which depends on the porosity, thickness and so on. R_{ct} and CPE_{dl} represent the charge transfer resistance and the *CPE* of electric double layer, respectively. The R_{ct} generally depends on the number and size of defects at the boundary between coating and substrate. The R_p is calculated from R_{coat} and R_{ct}, using Eq. 1.

$$\frac{1}{R_p} = \frac{1}{R_{coat}+R_{ct}} \qquad (1)$$

The circuit parameters were determined through curve fitting, and the fitted curves are shown in Fig. 4(a) and (b). The obtained parameters are summarized in Table 2, and the R_{coat}, R_{ct}, and R_p are plotted as a function of the carbonate content in Fig. 4(d)-(f).

In 0.9% NaCl solution, the R_p of Mg was improved more than 5000 times with the CAp coating, from approximately 25 Ω· cm^2 to 110-160 kΩ· cm^2. Both R_{coat} and R_{ct} slightly increased with the carbonate content, resulting in an approximately 1.5-fold increase in R_p. As shown in Table 2, both CPE_{coat}-*T* and CPE_{dl}-*T* tended to decrease with increasing carbonate content. The increase in R_{coat} and R_{ct} and decrease in CPE_{coat}-*T* and CPE_{dl}-*T* indicate a reduction in coating defects. However, the increase in R_p with the carbonate content was inconsistent to that of the I_{corr} (Fig. 2(e)). This

discrepancy between R_p and I_{corr} might be influenced by the characteristic known as the anomalous hydrogen evolution of Mg [49]. The details remain a subject for future investigation.

In Hanks' solution, the R_p of Mg was improved by more than 7 times with the CAp coating, from approximately 15 kΩ· cm^2 to 110–230 kΩ· cm^2. Both R_{coat} and R_{ct} increased with increasing carbonate content, resulting in an approximately 2-fold increase in R_p. Both CPE_{coat}-T and CPE_{dl}-T tended to decrease with increasing carbonate content (Table 2). The change in these impedance parameters indicates a reduction of coating defects. Eventually, it can be said that the corrosion protectiveness of the CAp coating increased with increasing carbonate content due to the decrease in coating defects.

The R_{coat} and R_{ct} of CAp-Mg were higher in Hanks' solution than those in 0.9% NaCl solution, indicating that the solution permeability and defects in the CAp coating in Hanks' solution was smaller than those in 0.9% NaCl solution. SEM-EDS analysis after EI measurements showed the deposition of calcium phosphate on the CAp1.0 coating in Hanks' solution (Fig. S3 and Table S2), suggesting that the defects in the CAp coating were repaired with deposited calcium phosphate. As a result, the R_p of CAp-Mg in Hanks' solution became higher than in 0.9% NaCl solution. This result was consistent with that of the I_{corr} (Fig. 3(e)).

The lowest R_{coat} of HAp-Mg in 0.9% NaCl solution indicates that the number and/or size of defects in the HAp coating were larger than those in the CAp coating. In contrast, in Hanks' solution, HAp-Mg exhibited the R_p equivalent to that of CAp1.0-Mg. Deposition of corrosion products containing calcium phosphate on HAp-Mg during anodic polarization in Hanks' solution (Fig. S2 and Table S1) suggests that the defects in the HAp coating were repaired by these corrosion products. However, no significant change in the surface morphology or composition of

the HAp coating was observed before and after EI measurements (Fig. S3 and Table S2), suggesting that the amount of deposited calcium phosphate during EI measurements was relatively small.

Consequently, it was found that the corrosion protectiveness of the CAp coating can be controlled by adjusting the carbonate content. This property is promising as a means to tailor the degradation rate of Mg devices depending on the patient's age, health condition and so on. On the other hand, the different results obtained in 0.9% NaCl and Hanks' solutions indicate that the corrosion protectiveness of the CAp coating is influenced by environmental factors, such as calcium phosphate deposition. In addition, we have reported that the corrosion protectiveness of HAp coating also depends on the composition of the Mg substrate [50]. Further investigation is required to precisely control the degradation rate of Mg devices in vivo by adjusting the carbonate content of the CAp coating.

3.4. Cell proliferation behavior on CAp-Mg and WE43

Figure 5 exhibits the whole surface optical images of CAp-Mg and WE43 and the glass with Giemsa-stained cells on Days 4, 8, and 15. Magnified Giemsa-stained images are shorn in Fig. S4. Calcein-PI fluorescence-stained images on Day 15 are shown in Fig. 6. Giemsa stains cells in purple regardless of their viability and calcein-PI stains living and dead cells in green and red, respectively. The accumulated amount of Mg^{2+} ions released in the medium at each time point during cell culturing, as well as the total amount of Mg^{2+} ions released over 15 days as a function of the carbonate content in the CAp coating, are shown in Fig. 7. For CAp-Mg, only CAp0.5- and CAp1.0-Mg on Day 15 obviously exhibited the presence of cells in the Giemsa-stained images

(Fig. 5(a)-(c) and Fig. S4(a)-(c)). In the calcein-PI-stained images, CAp0.25-Mg showed few cells, most of which were dead, CAp0.5-Mg showed a small number of cells, about half of which were alive, and CAp1.0-Mg showed numerous cells, most of which were alive (Fig. 6(a)-(c)). The Mg^{2+} ion release was significant from the beginning of cell culture for CAp0.25- and CAp0.5-Mg which increased with culturing period; whereas that from CAp1.0-Mg was suppressed up to Day 4 and gradually began between Days 4 and 8. The total amount of released Mg^{2+} ions of CAp1.0-Mg was about an order of magnitude smaller than that of CAp0.25- and CAp0.5-Mg (Fig. 7(c)). CAp0.25- and CAp0.5-Mg showed obvious corrosion on the disk edges from Day 4, while CAp1.0-Mg showed no obvious corrosion on Day 4. It was thus clearly demonstrated that the higher carbonate content in the CAp coating suppressed the substrate Mg corrosion, leading to the higher cell viable rate. Since most cells died on CAp0.25- and CAp0.5-Mg (Fig. 6(a)-(c)), the influence of the carbonate content on the osteoclastic response to the CAp coating could not be examined using CAp-Mg samples.

For CAp-WE43 and the glass (Fig. 5(d)-(g) and Fig. S4(d)-(g)), the Giemsa-stained images clearly demonstrated cell proliferation and colony formation up to Day 8, followed by the disappearance of colonies by Day 15. In contrast, the cells on the glass appeared to continue increasing up to Day 15 (Fig. 5(g) and Fig. S4(g)). A similar decrease in cell number from Day 8 to 15 was previously observed on the surface of CAp-WE43 with the higher carbonate contents than those in this study [31]. It was suggested that acids secreted by mature osteoclast cells corroded the underlying WE43 substrate, elevating the surrounding pH and causing the cell detachment [31]. The calcein-PI-stained images (Fig. 6(d)-(g)) show that most of the cells on CAp-WE43 were alive to a similar extent as on the glass surface. The amount of Mg^{2+} ions released from CAp-WE43 was one to two orders of magnitude lower than that from CAp-Mg (Fig. 7). In addition, no apparent

corrosion was observed on CAp-WE43, as shown in Fig. 5(d)-(f). Owing to its higher corrosion resistance, cells were able to proliferate on CAp-WE43.

The influence of the carbonate content in the CAp coating on the Mg^{2+} ion release behavior was not significant (Fig. 7(b) and (c)), although an improvement in the corrosion protectiveness of the CAp coating with increasing carbonate content was shown by the electrochemical tests in 0.9% NaCl and Hanks' solutions (Figs. 3 and 4). Biological corrosion factors, such as acid secretion from osteoclasts, presence of proteins, and the higher corrosion resistance of WE43 compared to pure Mg, might mask the effect of the carbonate content.

Most cells survived for 15 days regardless of the carbonate content in the CAp coating of WE43. Therefore, CAp-WE43 was mainly used to investigate the influence of the carbonate content on the osteoclastic response to the CAp coating.

3.5. Osteoclastic response to CAp-WE43

TRAP staining was performed to investigate the differentiation and mature of osteoclast precursors to osteoclasts. Osteoclast precursors differentiate into mononuclear osteoclasts, which mature into multinucleated giant cells. Differentiated osteoclasts express TRAP which is stained red in TRAP staining. Figure S5 shows the whole surface optical images of CAp-Mg and WE43 and the glass with TRAP-stained cells on Days 4, 8, and 15. The number of TRAP-positive cells was apparently smaller than that of Giemsa-stained cells, and even on CAp-WE43 surfaces at Day 8—where the most distinct colonies were observed with Giemsa staining (Fig. 5)—colonies were not clearly observed on the TRAP-stained surfaces (Fig. S5). Furthermore, very few TRAP-positive cells were observed on the glass surface. These results indicate that not all precursor cells

differentiated and matured into osteoclasts. Typical TRAP-stained images of CAp-WE43 and the glass on Days 4, 8, and 15 are shown in Fig. 8(a)-(d). Figure 8(e) and (f) presents the total number of TRAP-positive cells in the five fields of view and the mean area per cell (i.e., mean cell size) as a function of the culture period. Figure 9 shows magnified optical images and the corresponding topographic images relatively large TRAP-positive cells for CAp-Mg and CAp-WE43 on Days 4, 8, and 15.

Red-colored TRAP-positive cells were observed from Day 4 for all CAp-WE43 samples, and their number and size were comparable to those on the glass. The number of cells increased significantly up to Day 8 on CAp-WE43 samples but not on the glass (Fig. 8(e)), and this result is consistent with the increase in cell number observed in the Giemsa-stained CAp-WE43 samples (Fig. 5). The mean cell size on CAp-WE43, as obtained from the TRAP-stained images, did not change obviously between Day 4 and Day 8 and was similar to that on the glass (Fig. 8(f)). However, in the Giemsa-stained CAp-WE43 specimens (Fig. 5 and Fig. S4), two or three giant cells of 200–300 μm were observed in the colonies of CAp0.5- and CAp1.0-WE43 on Day 8, while such giant cells were not found on Day 4. It is considered that, due to the large number of small cells present in the TRAP-stained specimens on Day 8, the mean cell size became smaller, even though giant cells were present. On Day 8, TRAP-positive cells were clustered together in colony like formations on the whole surface images (Fig. S5(d)-(f)). These results indicate that osteoclast precursors proliferated and differentiated into osteoclasts up to Day 8 on CAp-WE43 samples. On Day 15, the whole surface images (Fig. S5) exhibited few relatively large TRAP-positive cells, while faintly red cells were observed in the high magnification images (Fig. 8(a-3)-(c-3) and (e)). On the other hand, the mean cell size increased, and the discolored regions similar in size to the cells appeared in the CAp coating (Fig. 8(f) and Fig. 9(a-5)-(c-5)). These facts indicate that the

proliferation and multinucleation of osteoclasts progressed up to around Day 8, after which mature osteoclasts each formed an actin ring on the surface to which they adhered and secreted acids within the ring between Days 8 and 15, leading to cell detachment.

The number of TRAP-positive cells on CAp-WE43 samples was clearly greater than that on the glass on Day 8 (Fig. 8(e) and Fig. S5). The Giemsa-stained images (Fig. 5 and Fig. S4) show that CAp0.5- and CAp1.0-WE43 exhibited giant cells within the colonies, whereas such large cells were not observed on the glass. These results indicate that the CAp coating further stimulates osteoclast differentiation in addition to the promotion by RANKL, since RANKL in the medium promotes osteoclast differentiation on the glass. On Day 15, mature cells appear to have detached from the CAp-coated surfaces. Therefore, the larger cell size observed on the glass surface at Day 15 does not imply that the glass surface is more supportive of osteoclast differentiation than the CAp-coated surfaces. Additionally, Fujioka-Kobayashi et al. reported that CAp provides a more favorable surface for osteoclast differentiation compared to deproteinized bovine bone mineral [(51)]. These findings suggest that the CAp coating enhances the proliferation and differentiation of osteoclasts, regardless of the carbonate content.

Figure 10 shows the total number of TRAP-positive cells and the mean cell size on Day 8 as functions of the carbonate content in the CAp coating. The results for CAp-Mg are also plotted, although these are based on very small numbers of cells. Both the number and the size of TRAP-positive cells increased with increasing carbonate content. Additionally, in the Giemsa-stained images, giant cells were observed within the colonies of CAp0.5- and CAp1.0-WE43, whereas no obvious giant cells were observed in CAp0.25-WE43 (Fig. 5 and Fig. S4). Therefore, these results demonstrate that the proliferation and maturation of osteoclast precursors are promoted by the increased carbonate content in the CAp coating.

3.6. Resorption behavior of CAp coating by osteoclasts

In evaluating the effect of the carbonate content on the osteoclastic resorption of the CAp coating, the following assumptions were made: (1) All TRAP-positive cells secrete acids and resorb the CAp coating; therefore, osteoclastic resorption occurs beneath the remaining TRAP-positive cells. (2) According to the topographical images shown in Fig. 9, resorption of the CAp coating results in the formation of concave regions on the surface. Thus, surface areas exhibiting concave features with shapes and sizes comparable to the cells were regarded as resorbed regions from which the cells had detached. Based on these assumptions, the sum of the areas beneath the remaining TRAP-positive cells and the identified concave regions was taken as the total resorbed area of the CAp coating.

To quantify these areas, 3D images, such as those shown in Fig. 11(a), were taken for five fields of view in each sample. The areas corresponding to the remaining cells and the concave regions were respectively measured using the analysis software equipped with the one-shot 3D profilometer. These measured areas in the five fields of view were then summed to determine the resorbed area of the CAp coating, as shown in Fig. 11(b). The resorbed area of the CAp coating on WE43 was approximately 1.5 times larger for the CAp1.0 than for the CAp0.25 and CAp0.5 coatings. On pure Mg, the osteoclastic resorption was clearly observed for the CAp1.0 coating which allowed the cell proliferation and osteoclastic differentiation.

Figure 11(c)-(e) shows the 3D images of the Giemsa-stained WE43 specimens. In all samples, a cell exhibiting a convex morphology was present at the center of each concave region. Because mature osteoclasts cannot be distinguished from other cells in the Giemsa-stained specimens, the

convex cells surrounded by concave areas were considered to be mature osteoclasts, and the concave regions were regarded as areas resorbed by osteoclasts. CAp0.25-, CAp0.5-, and CAp1.0-WE43 exhibited approximately 10, 17, and 15 concave regions, respectively. The size of the concave regions in CAp0.5- and CAp1.0-WE43 was relatively larger than that in CAp0.25-WE43. Furthermore, the CAp0.5- and CAp1.0-WE43 exhibited a similar number and size of the concave regions. The low-magnification 3D images of the TRAP-stained WE43 specimens shown in Fig. S6 exhibited a similar result to that of the Giemsa-stained samples.

These results demonstrate that the osteoclastic resorption of the CAp coating was enhanced by the increased carbonate content. This is attributed to the chemical property of CAp that the higher the carbonate content results in higher the solubility [44]. It remains to be further investigated whether the osteoclastic resorbability of the CAp coating on Mg changes with the carbonate content in vivo as it does in the present in vitro study.

4. Conclusions

The corrosion behavior of CAp0.25-, CAp0.5- and CAp1.0-Mg, containing approximately 11, 17, and 18 wt% carbonate, respectively, was examined by the polarization and EI tests in 0.9% NaCl and Hanks' solutions. Additionally, the response of osteoclasts to CAp0.25-, CAp0.5- and CAp1.0-Mg and WE43 samples, was evaluated. The findings are summarized as follows:

- In the polarization tests, the I_{corr} of CAp-Mg slightly increased with an increase in the carbonate content in 0.9% NaCl solution. On the contrary, in Hanks' solution, the I_{corr} slightly decreased with increasing carbonate content. The I_{corr} values in Hanks' solution were lower than those in 0.9% NaCl solution.

- In the EI tests, the CAp coating improved the R_p of Mg by more than 5000 times in 0.9% NaCl solution and more than 7 times in Hanks' solution. The R_p values in Hanks' solution were relatively higher than those in 0.9% NaCl solution.

- The R_p of CAp-Mg increased by 1.5 times in 0.9% NaCl solution and 2 times in Hanks' solution with increasing carbonate content, indicating a reduction in coating defects.

- In culturing osteoclast precursors, CAp1.0-Mg promoted cell proliferation and differentiation into osteoclasts, owing to the suppression of substrate Mg corrosion. In contrast, CAp0.25- and CAp0.5-Mg showed significant corrosion, resulting in reduced cell proliferation and differentiation.

- On CAp-WE43, proliferation and differentiation of osteoclast precursors into mature osteoclasts were enhanced with increasing carbonate content.

- The osteoclastic resorption area of the CAp coating increased by approximately 1.5 times with increased carbonate content.

In conclusion, this study demonstrates that the carbonate content of the CAp coating can be used to tailor the corrosion rate of biodegradable Mg alloy devices, such as bone screws, pins, and staples, to accommodate the patient's age, heath condition, and the implantation site. Because degradation of the CAp coating occurs after the induction of osteoclasts or osteoclast-like cells, the coating can maintain its corrosion protection ability until new bone or soft tissue is formed on its surface. Once these cells are induced, CAp coatings with higher carbonate content are resorbed more rapidly.

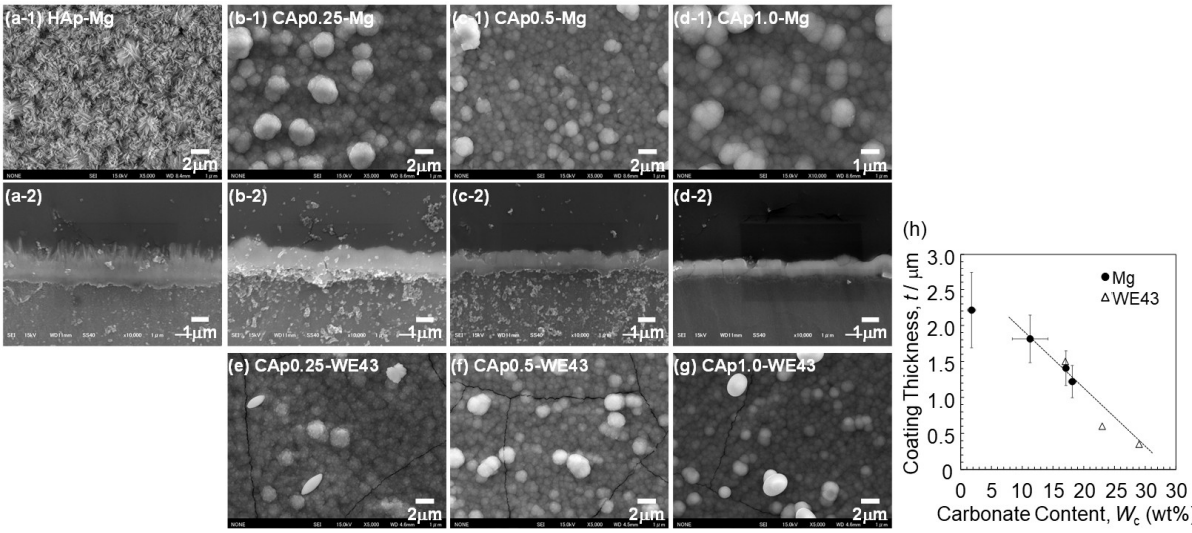

Figure 1. (a-1)-(d-1) and (e)-(g) Surface and (a-2)-(d-2) cross-sectional SEM images of (a) HAp-Mg, (b) CAp0.25-Mg, (c) CAp0.5-Mg, (d) CAp1.0-Mg, (e) CAp0.25-WE43, (f) CAp0.5-WE43 and (g) CAp1.0-WE43. (h) Coating thickness as a function of the carbonate content of HAp- and CAp-Mg. The coating thickness of CAp-WE43 is cited from ref. 38. Adopted from ref. 39, Fig. 1, with permission.

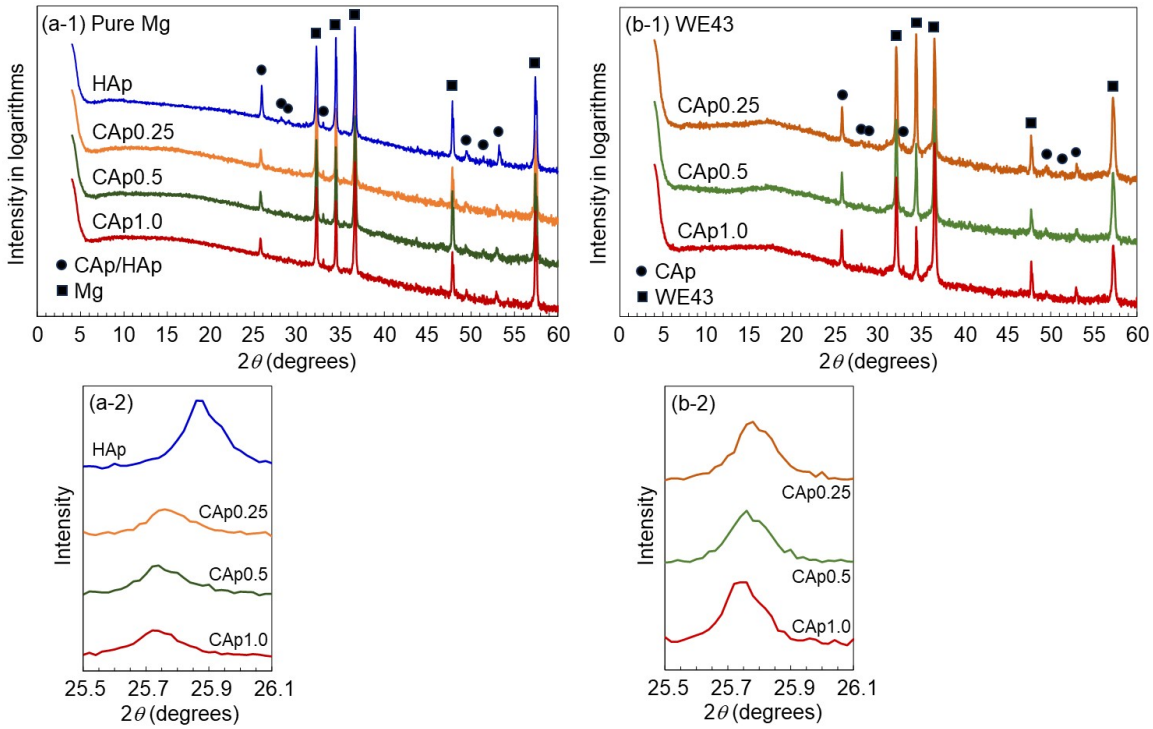

Figure 2. XRD patterns and magnified apatite 002 plane peak of (a) HAp- and CAp-Mg and (b) CAp-WE43. (a-1) and (b-1) Wide range XRD pattern and (a-2) and (b-2) magnified apatite 002 plane peak.

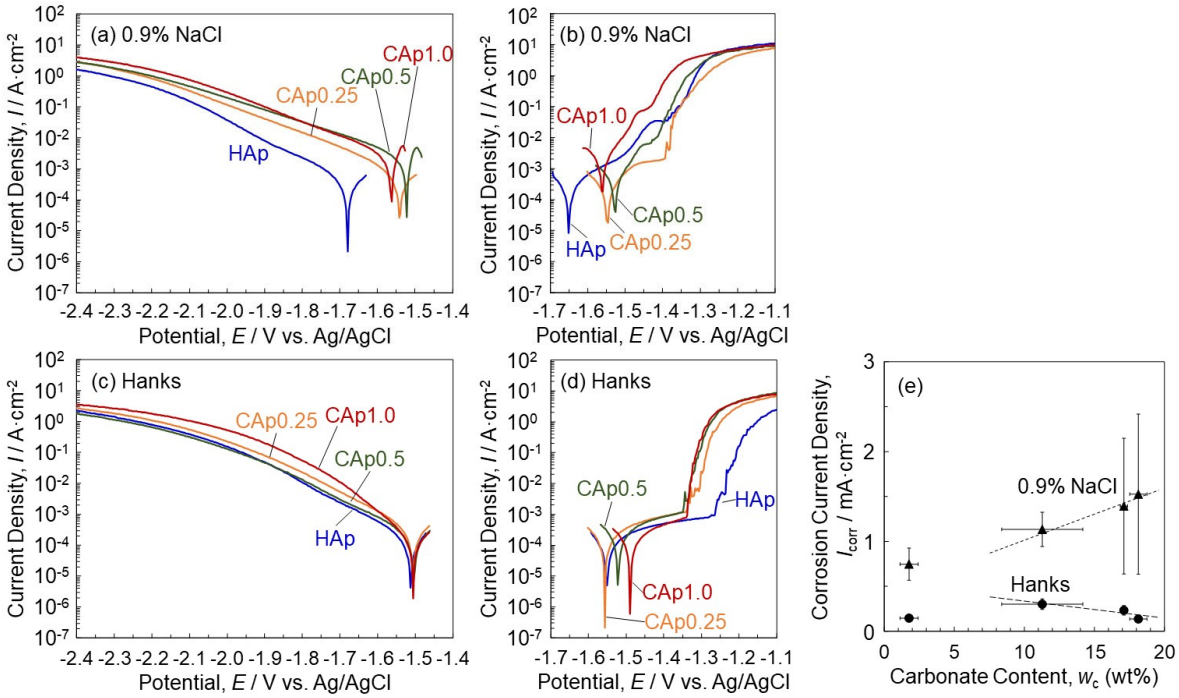

Figure 3. Potentiodynamic (a) and (c) cathodic and (b) and (d) anodic polarization curves of HAp- and CAp-Mg in (a) and (b) 0.9% NaCl and (c) and (d) Hanks' solutions. (e) I_{corr} as a function of the carbonate content of CAp-Mg.

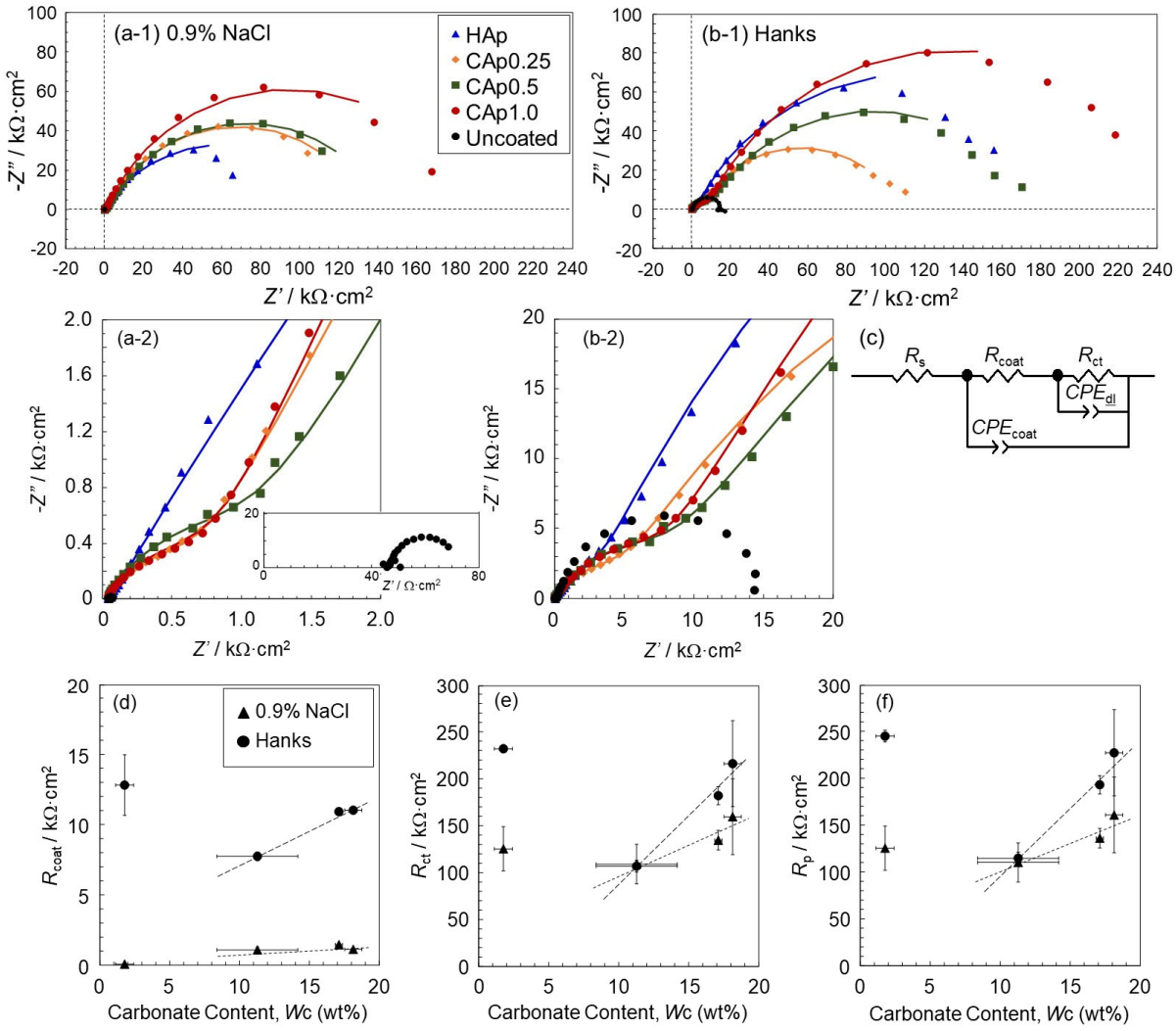

Figure 4. (a) and (b) Nyquist plots of HAp- and CAp-Mg in (a) 0.9% NaCl and (b) Hanks' solutions and (c) assumed equivalent circuit. (a-2) and (b-2) magnified plots of (a-1) and (b-1). The inset in (a-2) shows the Nyquist plot of uncoated Mg. (d) R_{coat}, (e) R_{ct}, and (f) R_p as a function of the carbonate content of HAp- and CAp-Mg in 0.9% NaCl and Hanks' solutions obtained by curve-fitting.

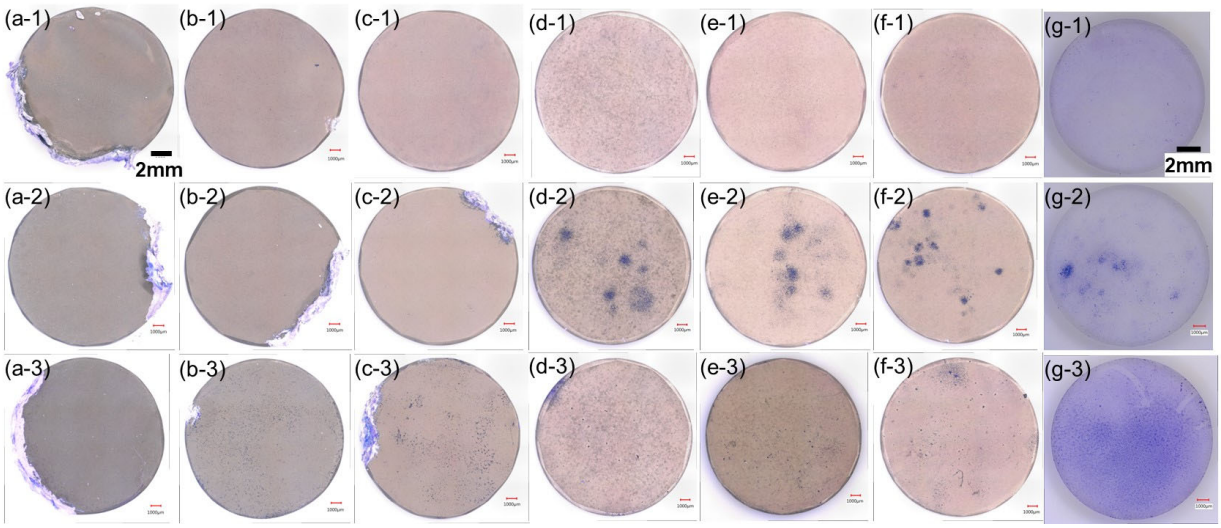

Figure 5. Optical surface images of (a) CAp0.25-Mg, (b) CAp0.5-Mg, (c) CAp1.0-Mg, (d) CAp0.25-WE43, (e) CAp0.5-WE43, (f) CAp1.0-WE43, and (g) glass with Giemsa-stained osteoclast cells. Images on (a-1)–(g-1) Day 4, (a-2)–(g-2) Day 8, and (a-3)–(g-3) Day 15. The sale bar for CAp-Mg and WE43 is shown in the image (a-1), and that for glass is shown in the image (g-1).

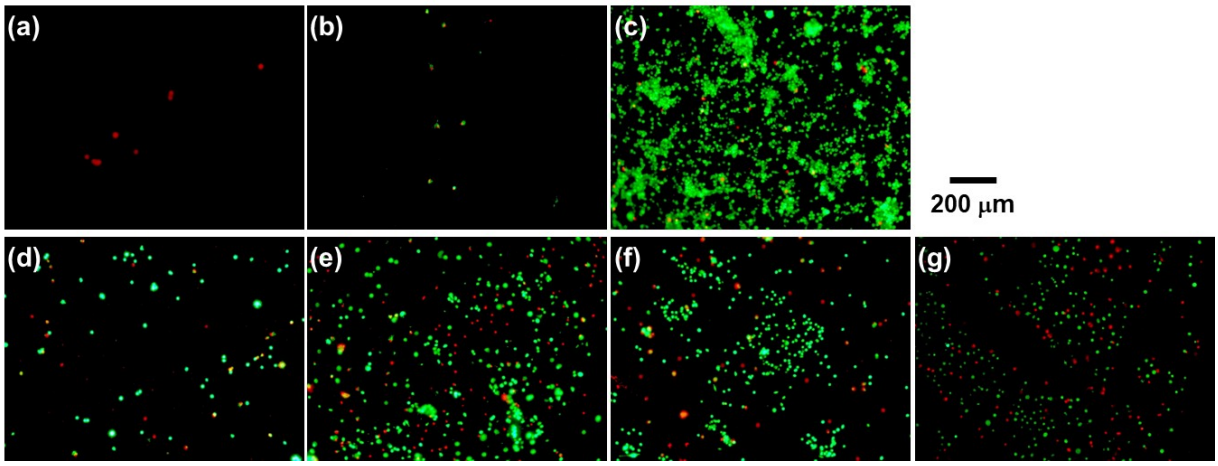

Figure 6. Composite fluorescence images of calcein- and PI-stained osteoclast cells on Day 15 of (a) CAp0.25-Mg, (b) CAp0.5-Mg, (c) CAp1.0-Mg, (d) CAp0.25-WE43, (e) CAp0.5-WE43, (f) CAp1.0-WE43, and (g) glass. Living cells, green; dead cells, red.

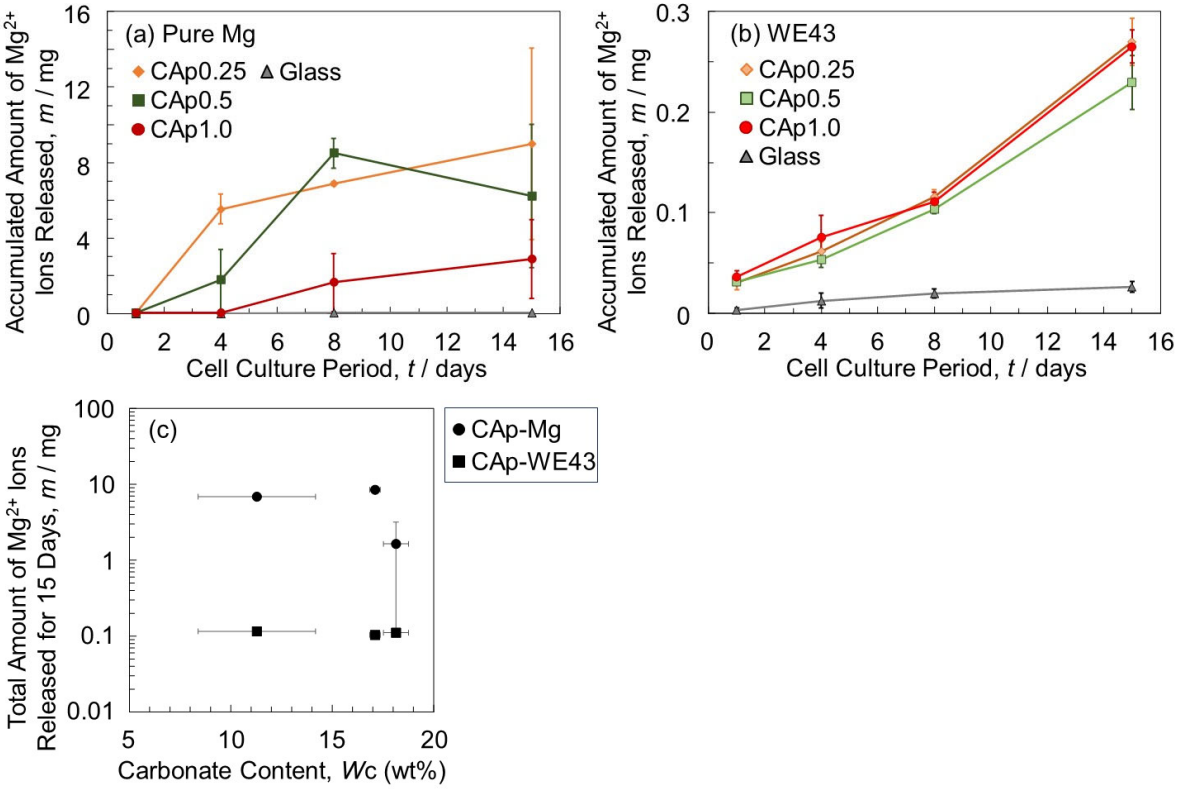

Figure 7. Accumulated amount of Mg^{2+} ions released from (a) CAp-Mg and (b) CAp-WE43 as a function of cell culture period. (c) Total amount of Mg^{2+} ions released for 15 days as a function of carbonate content.

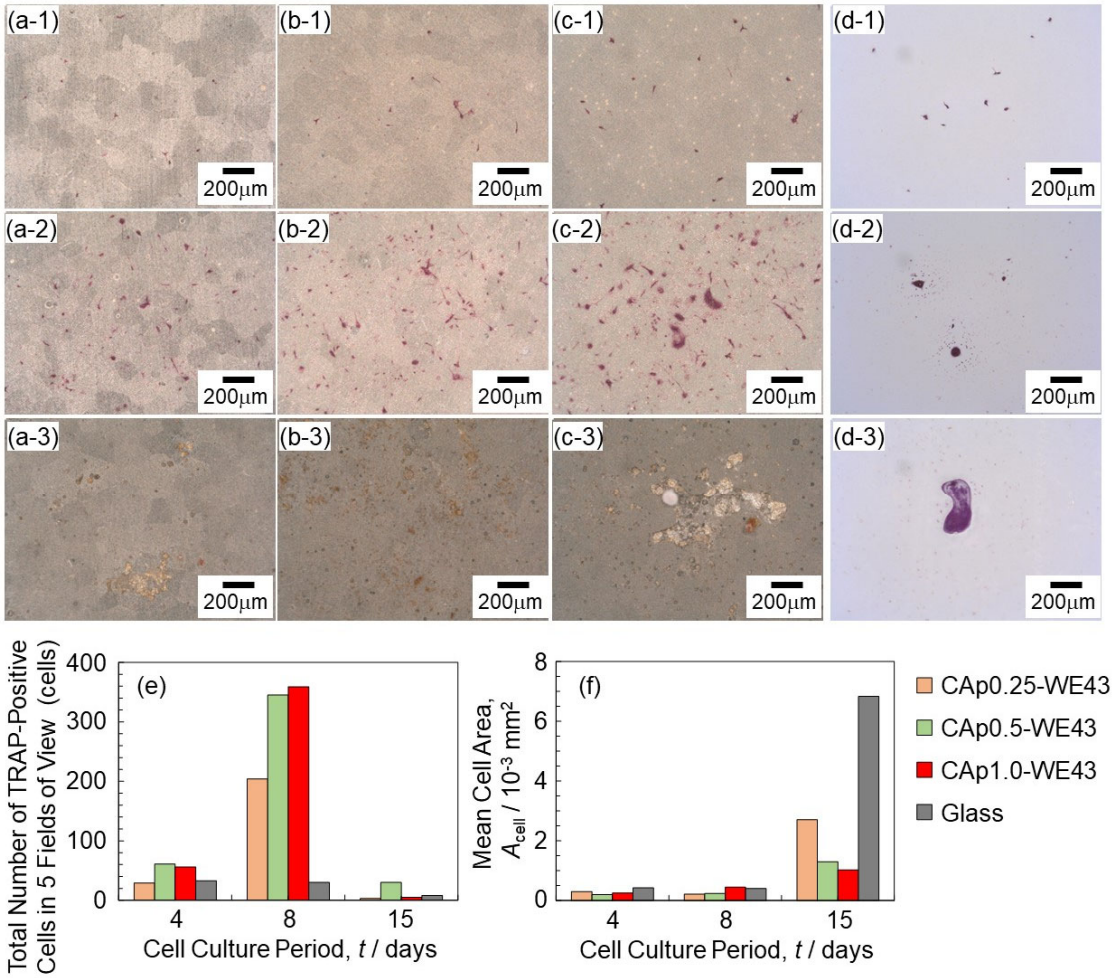

Figure 8. Optical surface images of (a) CAp0.25-WE43, (b) CAp0.5-WE43, (c) CAp1.0-WE43, and (d) glass with TRAP-stained osteoclast cells. Images on (a-1)–(d-1) Day 4, (a-2)–(d-2) Day 8, (a-3)–(d-3) Day 15. (e) Number of TRAP-positive cells (n=1) and (f) mean cell size as a function of cell culture period (n=1).

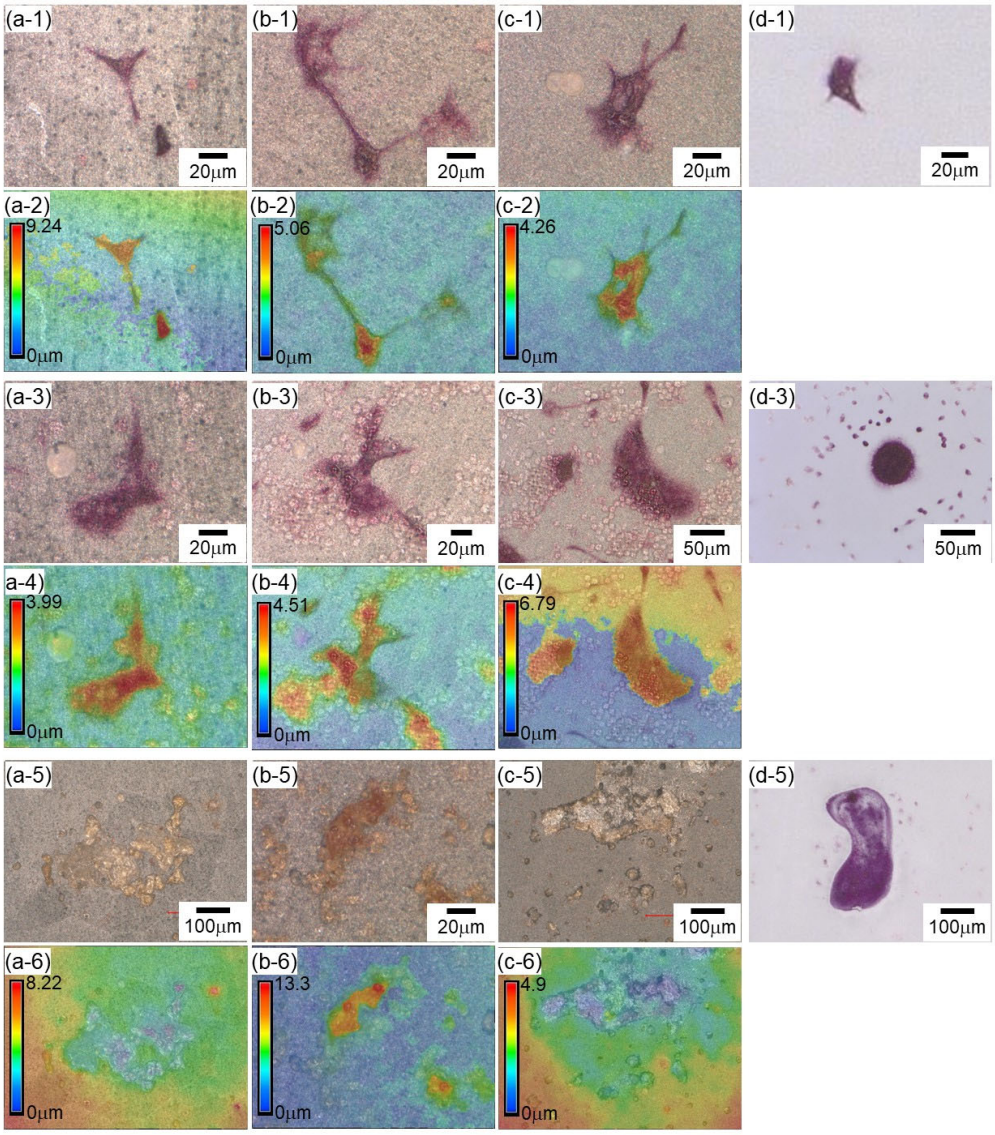

Figure 9. Optical images and corresponding topographic images of (a) CAp0.25-WE43, (b) CAp0.5-WE43, (c) CAp1.0-WE43, and (d) glass with TRAP-stained cells. (a-1)–(d-1), (a-3)–(d-3), and (a-5)–(d-5) Optical images and (a-2)–(d-2), (a-4)–(d-4), and (a-6)–(d-6) topographic images on (a-1)–(d-1) and (a-2)–(d-2) Day 4, (a-3)–(d-3) and (a-4)–(d-4) Day 8, (a-5)–(d-5) and (a-6)–(d-6) Day 15.

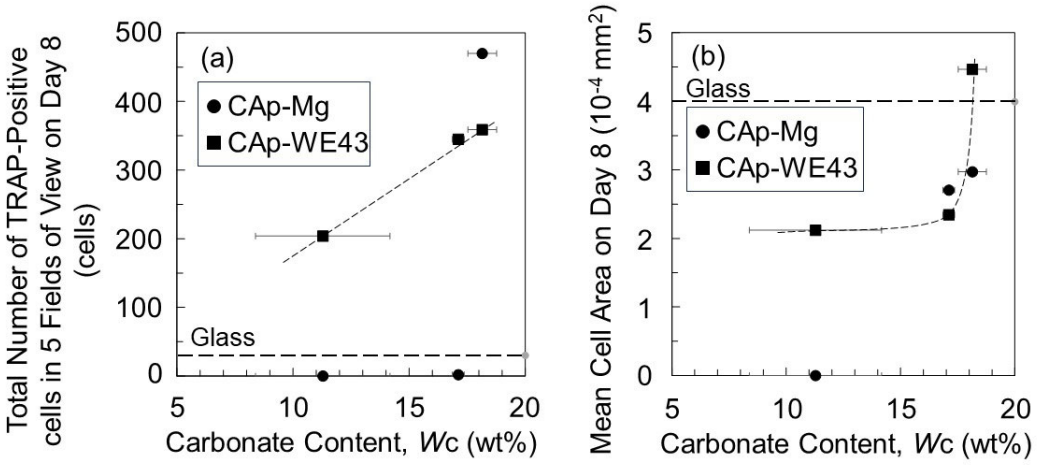

Figure 10. (a) Number of TRAP-positive cells and (b) mean cell size as a function of carbonate content of CAp-Mg and WE43.

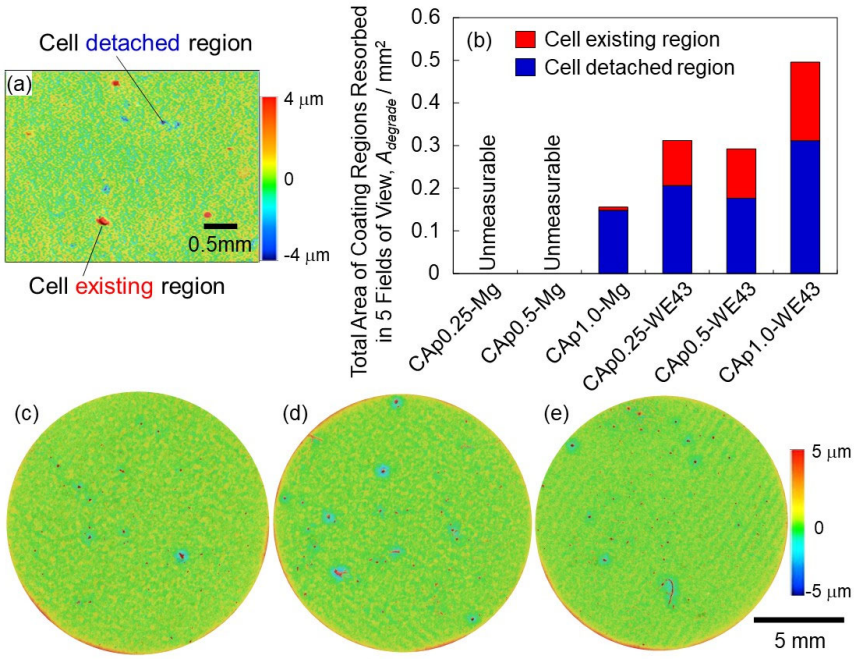

Figure 11. (a) Typical 3D image with osteoclasts on Day 15 of TRAP-stained CAp0.25-WE43. (b) Total area of regions where CAp coating was resorbed in five fields of view for CAp-Mg and CAp-WE43. 3D images on Day 15 of Giemsa-stained (c) CAp0.25-, (d) CAp0.5-, and (e) CAp1.0-WE43.

Table 1. Chemical composition of pure Mg and WE43 (mass%).

Material	Y	Nd	RE*	Fe	Si	Ni	Cu	Al
Pure Mg	-	-	-	0.0023	0.005	0.0002	0.0002	0.0049
WE43	4.0	2.3	1.1	0.001	-	0.000	0.002	-
	Cl	Pb	Zn	Zn+Ag	Li	Zr	IP**	Mg
Pure Mg	0.002	0.001	0.0055	-	-	-	-	Bal.
WE43	-	-	-	0.03	0.1	0.48	<0.01	Bal.

*RE: rare earths, **IP: impurities.

Table 2. Parameters in assumed equivalent electric circuit.

	Sample	R_s ($\Omega \cdot cm^2$)	R_{coat} ($k\Omega \cdot cm^2$)	CPE_{coat}-T ($\mu F \cdot s^{P-1} \cdot cm^2$)	CPE_{coat}-P (-)	R_{ct} ($k\Omega \cdot cm^2$)	CPE_{dl}-T ($\mu F \cdot s^{P-1} \cdot cm^2$)	CPE_{dl}-P (-)	R_p ($k\Omega \cdot cm^2$)
0.9% NaCl	HAp-Mg	38±3.8	0.81±0.65	4.1±0.002	0.87±0.16	125±23	13±0.16	0.65±0.01	125±24
	CAp0.25-Mg	31±4.6	1.1±0.19	3.0±0.84	0.66±0.02	109±21	6.9±0.072	0.71±0.01	110±21
	CAp0.5-Mg	312±3.0	1.5±0.062	1.4±0.37	0.71±0.01	135±11	7.4±0.58	0.69±0.01	136±10
	CAp1.0-Mg	34±8.2	1.1±0.079	2.1±0.48	0.67±0.02	160±40	4.2±0.34	0.76±0.01	161±40
Hanks	HAp-Mg	31±1.7	13±2.2	11±0.52	0.62±0.00	232±4.4	4.7±0.55	0.87±0.03	245±6.3
	CAp0.25-Mg	27±1.8	7.7±0.31	2.1±0.29	0.67±0.01	107±6.3	8.9±0.38	0.68±0.02	115±6.6
	CAp0.5-Mg	27±5.8	11±0.23	1.0±0.11	0.70±0.01	182±9.6	7.9±0.02	0.65±0.01	193±9.8
	CAp1.0-Mg	26±3.5	11±0.24	1.4±0.32	0.68±0.01	216±46	5.1±0.35	0.75±0.01	227±46

Corresponding Author

Sachiko Hiromoto - Research Center for Structural Materials, National Institute for Materials Science, Tsukuba 305-0047, Japan

https://orcid.org/0000-0003-4666-6708

Email: HIROMOTO.Sachiko@nims.go.jp

Authors

Kazuma Midorikawa - Faculty of Science and Engineering, Waseda University, Tokyo, 169-8555, Japan

Research Center for Structural Materials, National Institute for Materials Science, Tsukuba 305-0047, Japan

† Present Affiliation: Nippon Steel Corporation

Tomohiko Yamazaki - Research Center for Macromolecules and Biomaterials, National Institute for Materials Science, Tsukuba, 305-0047, Japan

Tomoyuki Yamamoto - Faculty of Science and Engineering, Waseda University, Tokyo, 169-8555, Japan

Kagami Memorial Research Institute for Materials Science and Technology, Tokyo 169-0051, Japan

Author Contributions

The manuscript was written through the contributions of all authors. All authors have approved the final version of the manuscript.

Acknowledgements

We would like to thank Dr. Shobo for her helpful cell culture experimentation. This work was mostly supported by JSPS Grant-in-Aid for Scientific Research (B) Grant Number 23K23066. This work was supported by "Advanced Research Infrastructure for Materials and Nanotechnology in Japan (ARIM)" of the Ministry of Education, Culture, Sports, Science and Technology (MEXT). Proposal Number JPMXP1224NM5085.

Supporting Information: FTIR spectra for HAp- and CAp-Mg samples, SEM images and EDS surface composition of HAp- and CAp-Mg samples after anodic polarization and EI measurements, high-magnification optical surface images of Giemsa-stained CAp-Mg and CAp-WE43, low-magnification optical surface images of TRAP-stained CAp-Mg and CAp-WE43, and low-magnification 3D images of CAp-WE43.

References

(1) Witte, F. The history of biodegradable magnesium implants: A review. *Acta Biomater.* **2010,** *6* (5), 1680-1692, DOI: DOI 10.1016/j.actbio.2010.02.028.

(2) Zeng, R. C.; Dietzel, W.; Witte, F.; Hort, N.; Blawert, C. Progress and Challenge for Magnesium Alloys as Biomaterials. *Adv. Biomater.* **2008,** *10* (8), B3-B14, DOI: 10. 1002/adem.200800035.

(3) Hornberger, H.; Virtanen, S.; Boccaccini, A. R. Biomedical coatings on magnesium alloys - A review. *Acta Biomater.* **2012,** *8* (7), 2442-2455, DOI: 10.1016/j.actbio.2012.04.012.

(4) Treiser, M.; Abramson, S.; Langer, R.; Kohn, J. Degradable and Resorbable Biomaterials. In *Biomaterials Science: An Introduction to Materials in Medicine Third Edition*; Ratner, B. D.; Hoffman, A. S.; Schoen, F. J.; Lemons, J. E., Eds.; Elsevier: MA, USA, 2013; Chapter 1.2.6, pp 179-195.

(5) Zhao, D.; Witte, F.; Lu, F.; Wang, J.; Li, J.; Qin, L. Current status on clinical applications of magnesium-based orthopaedic implants: A review from clinical translational perspective. *Biomaterials* **2017,** *112*, 287-302, DOI: 10.1016/j.biomaterials.2016.10.017.

(6) Niranjan, C. A.; Raghavendra, T.; Rao, M. P.; Siddaraju, C.; Gupta, M.; Jain, V. K. S.; Aishwarya, R. Magnesium alloys as extremely promising alternatives for temporary orthopedic implants - A review. *Journal of Magnesium and Alloys* **2023,** *11* (8), 2688-2718, DOI: 10.1016/j.jma.2023.08.002.

(7) Zhou, Y.; Zhang, A.; Wu, J.; Guo, S.; Sun, Q. Application and Perspectives: Magnesium Materials in Bone Regeneration. *ACS Biomater Sci Eng* **2024,** *10* (6), 3514-3527, DOI: 10.1021/acsbiomaterials.3c01713.

(8) Kuwahara, H.; Al-Abdullat, Y.; Mazaki, N.; Tsutsumi, S.; Aizawa, T. Precipitation of magnesium apatite on pure magnesium surface during immersing in Hank's solution. *Mater. Trans.* **2001,** *42* (7), 1317-1321, DOI: 10.2320/matertrans.42.1317.

(9) Al-Abdullat, Y.; Tsutsumi, S.; Nakajima, N.; Ohta, M.; Kuwahara, H.; Ikeuchi, K. Surface modification of magnesium by $NaHCO_3$ and corrosion behavior in Hank's solution for new biomaterial applications. *Mater. Trans.* **2001,** *42* (8), 1777-1780, DOI: 10.2320/matertrans.42.1777.

(10) Haude, M.; Erbel, R.; Erne, P.; Verheye, S.; Degen, H.; Bose, D.; Vermeersch, P.; Wijnbergen, I.; Weissman, N.; Prati, F.; Waksman, R.; Koolen, J. Safety and performance of the drug-eluting absorbable metal scaffold (DREAMS) in patients with de-novo coronary lesions: 12 month results ofthe prospective, multicentre, first-in-man BIOSOLVE-I trial. *Lancet* **2013,** *381* (9869), 836-844, DOI: 10. 1016/S0140-6736(12)61765-6.

(11) Plaass, C.; Ettinger, S.; Sonnow, L.; Koenneker, S.; Noll, Y.; Weizbauer, A.; Reifenrath, J.; Claassen, L.; Daniilidis, K.; Stukenborg-Colsman, C.; Windhagen, H. Early results using a biodegradable magnesium screw for modified chevron osteotomies. *J. Orthop. Res.* **2016,** *34* (12), 2207-2214, DOI: 10.1002/jor.23241.
(12) Seitz, J. M.; Lucas, A.; Kirschner, M. Magnesium-Based Compression Screws: A Novelty in the Clinical Use of Implants. *Jom* **2016,** *68* (4), 1177-1182, DOI: 10.1007/s11837-015-1773-1.
(13) Waksman, R.; Zumstein, P.; Pritsch, M.; Wittchow, E.; Haude, M.; Lapointe-Corriveau, C.; Leclerc, G.; Joner, M. Second-generation magnesium scaffold Magmaris: device design and preclinical evaluation in a porcine coronary artery model. *EuroIntervention* **2017,** *13* (4), 440-449, DOI: 10.4244/EIJ-D-16-00915.
(14) Haude, M.; Ince, H.; Kische, S.; Abizaid, A.; Tolg, R.; Alves Lemos, P.; Van Mieghem, N. M.; Verheye, S.; von Birgelen, C.; Christiansen, E. H.; Wijns, W.; Garcia-Garcia, H. M.; Waksman, R. Sustained safety and clinical performance of a drug-eluting absorbable metal scaffold up to 24 months: pooled outcomes of BIOSOLVE-II and BIOSOLVE-III. *EuroIntervention* **2017,** *13* (4), 432-439, DOI: 10.4244/EIJ-D-17-00254.
(15) Naujokat, H.; Seitz, J. M.; Acil, Y.; Damm, T.; Moller, I.; Gulses, A.; Wiltfang, J. Osteosynthesis of a cranio-osteoplasty with a biodegradable magnesium plate system in miniature pigs. *Acta Biomater.* **2017,** *62*, 434-445, DOI: 10.1016/j.actbio.2017.08.031.
(16) Joner, M.; Ruppelt, P.; Zumstein, P.; Lapointe-Corriveau, C.; Leclerc, G.; Bulin, A.; Castellanos, M. I.; Wittchow, E.; Haude, M.; Waksman, R. Preclinical Evaluation of Degradation Kinetics and Elemental Mapping of First and Second Generation Bioresorbable Magnesium Scaffolds. *EuroIntervention* **2018,** *14* (9), e1040-e1048, DOI: 10.4244/EIJ-D-17-00708.
(17) Byun, S. H.; Lim, H. K.; Cheon, K. H.; Lee, S. M.; Kim, H. E.; Lee, J. H. Biodegradable magnesium alloy (WE43) in bone-fixation plate and screw. *Journal of biomedical materials research. Part B, Applied biomaterials* **2020,** *108B*, 2505-2512, DOI: 10.1002/jbm.b.34582.
(18) Plaass, C.; von Falck, C.; Ettinger, S.; Sonnow, L.; Calderone, F.; Weizbauer, A.; Reifenrath, J.; Claassen, L.; Waizy, H.; Daniilidis, K.; Stukenborg-Colsman, C.; Windhagen, H. Bioabsorbable magnesium versus standard titanium compression screws for fixation of distal metatarsal osteotomies - 3 year results of a randomized clinical trial. *J. Orthop. Sci.* **2018,** *23* (2), 321-327, DOI: 10.1016/j.jos.2017.11.005.

(19) Clark, D.; Nakamura, M.; Miclau, T.; Marcucio, R. Effects of Aging on Fracture Healing. *Curr. Osteoporos. Rep.* **2017,** 15 (6), 601-608, DOI: 10.1007/s11914-017-0413-9.
(20) Sathyendra, V.; Darowish, M. Basic science of bone healing. *Hand Clin.* **2013**, 29 (4), 473-481, DOI: 10.1016/j.hcl.2013.08.002.
(21) Hiromoto, S.; Shishido, T.; Yamamoto, A.; Maruyama, N.; Somekawa, H.; Mukai, T. Precipitation control of calcium phosphate on pure magnesium by anodization. *Corros. Sci.* **2008,** *50* (10), 2906-2913, DOI: DOI 10.1016/j.corsci.2008.08.013.
(22) Li, L.; Zhang, M.; Li, Y.; Zhao, J.; Qin, L.; Lai, Y. X. Corrosion and biocompatibility improvement of magnesium-based alloys as bone implant materials: a review. *Regenerative Biomaterials* **2017,** *4* (2), 129-137, DOI: 10.1093/rb/rbx004.
(23) Cipriano, A. F.; Lin, J.; Miller, C.; Lin, A.; Cortez Alcaraz, M. C.; Soria, P., Jr.; Liu, H. Anodization of magnesium for biomedical applications - Processing, characterization, degradation and cytocompatibility. *Acta Biomater.* **2017,** *62*, 397-417, DOI: 10.1016/j.actbio.2017.08.017.
(24) Kamrani, S.; Fleck, C. Biodegradable magnesium alloys as temporary orthopaedic implants: a review. *Biometals* **2019,** *32* (2), 185-193, DOI: 10.1007/s10534-019-00170-y.
(25) Zhang, A.-M.; Lenin, P.; Zeng, R.-C.; Kannan, M. B. Advances in hydroxyapatite coatings on biodegradable magnesium and its alloys. *J. Magnes. Alloys* **2022,** *10* (5), 1154-1170, DOI: 10.1016/j.jma.2022.01.001.
(26) Gnedenkov, A. S.; Sinebryukhov, S. L.; Filonina, V. S.; Gnedenkov, S. V. Hydroxyapatite-containing PEO-coating design for biodegradable Mg-0.8Ca alloy: Formation and corrosion behaviour. *J. Magnes, Alloys* **2023,** *11* (12), 4468-4484, DOI: 10.1016/j.jma.2022.12.002.
(27) Li, L.; Zhang, Z.; Zhang, D.; Qi, F.; Dai, Y.; Wei, W; Ouyang, X. Effects of metal ion implantation (Fe, Ti, Zn and Zr) on mechanical properties, corrosion resistance and biocompatibility of WE43 Mg alloy. *J. Magnes. Alloys* **2025,** *13* (1), 296-310, DOI: 10.1016/j.jma.2024.05.005.
(28) Wang, X.; Guo, L.; Liu, X.; Dai, Y.; She, J.; Zhang, D.; Qi, F.; Wei, W.; Ouyang, X. Enhanced corrosion resistance and cell activity of magnesium alloy by DCPD/MgHPO4?3H2O coating via one-step chemical conversion. *Surf. Coat. Technol.* **2024,** *476*, 130228, DOI: 10.1016/j.surfcoat.2023.130228.

(29) Sheng, Y.; Li, W.; Chai, Y.; Yin, S.; Li, J.; Guan, S. A compound Schiff base coating on biomedical magnesium alloy for enhanced corrosion resistance and biocompatibility. *Smart Mater. Manufac.* **2023,** *1*, 100003, DOI: 10.1016/j.smmf.2022.100003.
(30) Kasuga, T. Coatings for metallic biomaterials. In *Metals for biomedical devices*; Niinomi, M., Ed.; Woodhead Publishing Limited: Camridge(UK), 2010; Chapter 11, pp 260-282.
(31) Kikuchi, M.; Ikoma, T.; Itoh, S.; Matsumoto, H. N.; Koyama, Y.; Takakuda, K.; Shinomiya, K.; Tanaka, J. Biomimetic synthesis of bone-like nanocomposites using the self-organization mechanism of hydroxyapatite and collagen. *Compos. Sci. Technol.* **2004,** *64* (6), 819-825, DOI: 10.1016/j.compscitech.2003.09.002.
(32) Kokubo, T.; Yamaguchi, S. Novel bioactive materials developed by simulated body fluid evaluation: Surface-modified Ti metal and its alloys. *Acta Biomater.* **2016,** *44*, 16-30, DOI: 10.1016/j.actbio.2016.08.013.
(33) Akita, K.; Fukuda, N.; Kamada, K.; Kudoh, K.; Kurio, N.; Tsuru, K.; Ishikawa, K.; Miyamoto, Y. Fabrication of porous carbonate apatite granules using microfiber and its histological evaluations in rabbit calvarial bone defects. *J. Biomed. Mater. Res. A* **2020,** *108* (3), 709-721, DOI: 10.1002/jbm.a.36850.
(34) Feng, B.; Chen, J. Y.; Qi, S. K.; He, L.; Zhao, J. Z.; Zhang, X. D. Carbonate apatite coating on titanium induced rapidly by precalcification. *Biomaterials* **2002,** *23* (1), 173-9, DOI: 10.1016/s0142-9612(01)00093-x.
(35) Shi, R.; Hayashi, K.; Ishikawa, K. Rapid Osseointegration Bestowed by Carbonate Apatite Coating of Rough Titanium. *Adv.Mater. Interfaces* **2020,** *7* (18), DOI: 10.1002/admi.202000636.
(36) Nagayama, M.; Takeuchi, H.; Doi, Y. Comparison of carbonate apatite and beta-tricalcium phosphate (resorbable calcium phosphates) implanted subcutaneously into the back of rats. *Dent. Mater. J.* **2006,** *25* (2), 219-225, DOI: 10.4012/dmj.25.219.
(37) Hiromoto, S. High corrosion resistance of magnesium coated with hydroxyapatite directly synthesized in an aqueous solution. *Electrochim. Acta* **2009,** *54* (27), 7085-7093, DOI: 10.1016/j.electacta.2009.07.033.
(38) Hiromoto, S.; Itoh, S.; Noda, N.; Yamazaki, T.; Katayama, H.; Akashi, T. Osteoclast and osteoblast responsive carbonate apatite coatings for biodegradable magnesium alloys. *Sci. Technol. Adv. Mater.* **2020,** *21* (1), 346–358, DOI: 10.1080/14686996.2020.1761237.

(39) Midorikawa, K.; Hiromoto, S.; Yamamoto, T. Carbonate content control in carbonate apatite coatings of biodegradable magnesium. *Ceram. Int.* **2024,** *50* (4), 6784-6792, DOI: 10.1016/j.ceramint.2023.12.021.
(40) Tomozawa, M.; Hiromoto, S. Microstructure of hydroxyapatite- and octacalcium phosphate-coatings formed on magnesium by a hydrothermal treatment at various pH values. *Acta Mater.* **2011,** *59* (1), 355-363, DOI: 10.1016/j.actamat.2010.09.041.
(41) Hiromoto, S.; Inoue, M.; Taguchi, T.; Yamane, M.; Ohtsu, N. In vitro and in vivo biocompatibility and corrosion behaviour of a bioabsorbable magnesium alloy coated with octacalcium phosphate and hydroxyapatite. *Acta Biomater.* **2015,** *11*, 520-30, DOI: 10.1016/j.actbio.2014.09.026.
(42) Ngo, T. T. A.; Hiromoto, S.; Do, L. C.; Pham, H. H.; Hanh, L. Effect of pH of coating solution on the adhesion strength and corrosion resistance of hydroxyapatite and octacalcium phosphate coated WE43 alloy. *J. Biomater. Appl.* **2021**, 8853282211012525, DOI: 10.1177/08853282211012525.
(43) Hiromoto, S.; Nozoe, E.; Hanada, K.; Yoshimura, T.; Shima, K.; Nakamura, N.; Chiba, A. Comparative Degradation Behavior of Carbonate Apatite-Coated and Hydroxyapatite-Coated Mg-Ca Alloy Plates and Screws in Rabbit Femurs. *Biomed.l Mater. Devices* **2024**, 3 (2), 1183-1199, DOI: 10.1007/s44174-024-00217-w.
(44) Suetsugu, Y. Carbonate Ions in Apatite Structure. *Inorganic Materials* **1996,** *3* (1), 48-54, DOI: 10.11451/mukimate1994.3.48.
(45) Nakamura, M.; Hiratani, R.; Hentunen, T.; Salonen, J.; Yamashita, K. Hydroxyapatite with High Carbonate Substitutions Promotes Osteoclast Resorption through Osteocyte-like Cells. *ACS Biomater. Sci. Eng.* **2016,** *2* (2), 259-267, DOI: 10.1021/acsbiomaterials.5b00509.
(46) Hiromoto, S.; Itoh, S.; Doi, K.; Katayama, H.; Akashi, T. Short- and long-term corrosion behavior of carbonate apatite-coated Mg-4mass% Y-3mass% RE alloy in cell culture medium. *Corros. Sci.* **2022,** *200*, 110222, DOI: 10.1016/j.corsci.2022.110222.
(47) Ohtsuka, M.; Matsuda, Y. Physicochemical Properties of Synthetic Apatite and its Application Study as Biomaterials. *Journal of the Association of Materials Engneering for Resources* **1991,** *4* (2), 128-141, DOI: 10.5188/jsmerj.4.2_128.

(48) Hiromoto, S. Self-healing property of hydroxyapatite and octacalcium phosphate coatings on pure magnesium and magnesium alloy. *Corros. Sci.* **2015,** *100*, 284-294, DOI: 10.1016/j.corsci.2015.08.001.
(49) Esmaily, M.; Svensson, J. E.; Fajardo, S.; Birbilis, N.; Frankel, G. S.; Virtanen, S.; Arrabal, R.; Thomas, S.; Johansson, L. G. Fundamentals and advances in magnesium alloy corrosion. *Prog. Mater. Sci.* **2017,** *89*, 92-193, DOI: 10.1016/j.pmatsci.2017.04.011.
(50) Hiromoto, S.; Nozoe, E.; Hanada, K.; Yoshimura, T.; Shima, K.; Kibe, T.; Nakamura, N.; Doi, K. In vivo degradation and bone formation behaviors of hydroxyapatite-coated Mg alloys in rat femur. *Mater. Sci. Eng. C.* **2021,** 122, 111942, DOI: 10.1016/j.msec.2021.111942.
(51) Fujioka-Kobayashi, M.; Miyamoto, Y.; Ishikawa, K.; Satomi, T.; Schaller, B. Osteoclast behaviors on the surface of deproteinized bovine bone mineral and carbonate apatite substitutes in vitro. *J. Biomed. Mater. Res. A* **2022,** *110* (8), 1524-1532, DOI: m10.1002/jbm.a.37392.

TOC Graphic

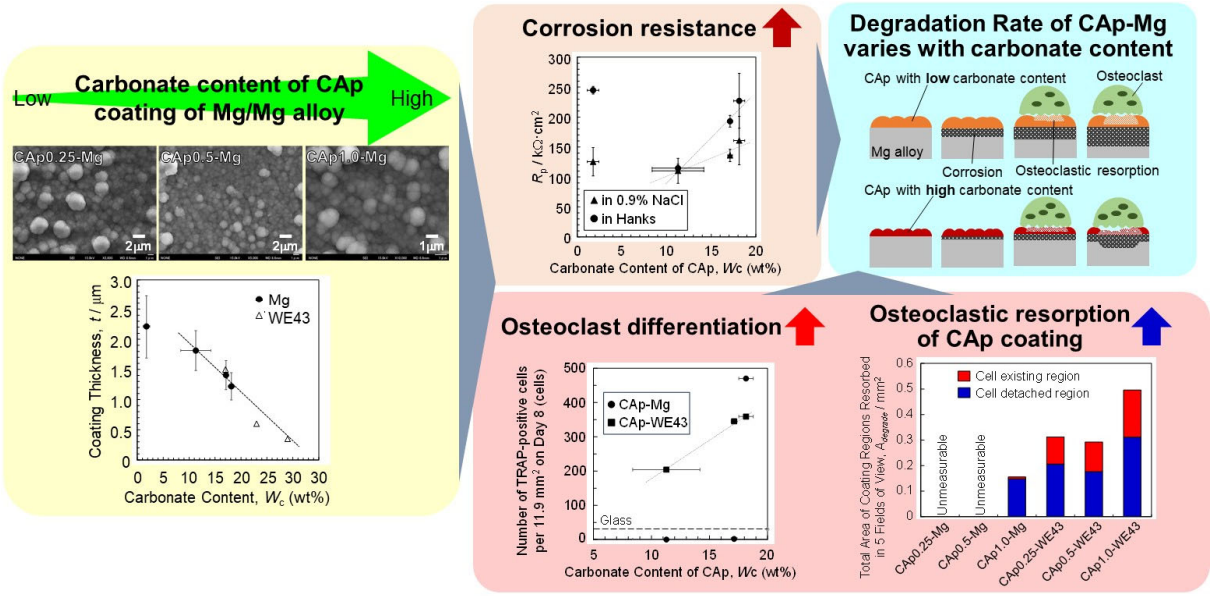
Low
Carbonate content of CAp coating of Mg/Mg alloy
High
CAp0.25-Mg
CAp0.5-Mg
CAp1.0-Mg
2μm
2μm
1μm
Coating Thickness, t / μm
Carbonate Content, Wc (wt%)
Mg
WE43
Corrosion resistance
Rp / kΩ·cm2
in 0.9% NaCl
in Hanks
Carbonate Content of CAp, Wc (wt%)
Degradation Rate of CAp-Mg varies with carbonate content
CAp with low carbonate content
Osteoclast
Mg alloy
Corrosion
Osteoclastic resorption
CAp with high carbonate content
Osteoclast differentiation
Number of TRAP-positive cells per 11.9 mm2 on Day 8 (cells)
CAp-Mg
CAp-WE43
Glass
Carbonate Content of CAp, Wc (wt%)
Osteoclastic resorption of CAp coating
Total Area of Coating Regions Resorbed in 5 Fields of View, Aresorb / mm2
Cell existing region
Cell detached region
Unmeasurable
Unmeasurable
CAp0.25-Mg
CAp0.5-Mg
CAp1.0-Mg
CAp0.25-WE43
CAp0.5-WE43
CAp1.0-WE43